

Mars without the equilibrium rotational figure, Tharsis, and the remnant rotational figure

I. Matsuyama¹ and M. Manga¹

Received 29 June 2010; revised 24 September 2010; accepted 13 October 2010; published 31 December 2010.

[1] We use a revised partitioning of the planet figure into equilibrium and nonequilibrium contributions that takes into account the presence of an elastic lithosphere to study the Martian gravity field and shape. The equilibrium contribution is associated with the present rotational figure, and the nonequilibrium contribution is dominated by Tharsis and a remnant rotational figure supported by the elastic lithosphere that traces the paleopole location prior to the formation of Tharsis. We calculate the probability density functions for Tharsis' size and location, the paleopole location, and the global average thickness of the elastic lithosphere at the time Tharsis was emplaced. Given the observed degree-3 spherical harmonic gravity coefficients, the expected Tharsis center location is $258.6 \pm 4.2^\circ\text{E}$, $9.8 \pm 0.9^\circ\text{N}$, where the uncertainties represent the 90% confidence interval. Given this Tharsis center location and the observed degree-2 spherical harmonic gravity coefficients, the expected paleopole location prior to the emplacement of Tharsis is $259.5 \pm 49.5^\circ\text{E}$, $71.1^{+17.5}_{-14.4}^\circ\text{N}$, and the expected elastic lithospheric thickness at the time of loading is 58^{+34}_{-32} km. Our estimated paleopole colatitude implies $18.9^{+14.4}_{-17.5}^\circ$ of true polar wander (TPW) driven by the emplacement of Tharsis, in disagreement with previous studies that invoke large TPW. The remnant rotational figure is visible in both the nonequilibrium degree-2 geoid (areoid) without Tharsis and the nonequilibrium degree-2 topography without Tharsis. The remnant rotational figure is also visible in the total nonequilibrium geoid without Tharsis, but it is not visible in the total nonequilibrium topography without Tharsis due to the strong signal of the north-south dichotomy. Shorter wavelength geological features become significantly more visible in the geoid with the removal of the long wavelength contributions of the equilibrium rotational figure, Tharsis, and the remnant rotational figure. Removal of the equilibrium rotational figure and Tharsis from the topography reveals a better defined north-south dichotomy boundary.

Citation: Matsuyama, I., and M. Manga (2010), Mars without the equilibrium rotational figure, Tharsis, and the remnant rotational figure, *J. Geophys. Res.*, 115, E12020, doi:10.1029/2010JE003686.

1. Introduction

[2] The gravitational figure of planetary bodies is commonly partitioned into hydrostatic and nonhydrostatic contributions (hereafter nonhydrostatic theory). In this case, under the assumption that the planet has no long-term rigidity, the hydrostatic contribution corresponds to the rotational figure assuming hydrostatic equilibrium. The remaining gravitational figure comprises the nonhydrostatic contribution. However, the nonhydrostatic theory is generally not suitable for planets with an elastic lithosphere like Mars. *Bills and James* [1999] noted that the present Martian rotational state is unstable in the framework of the nonhydrostatic theory. *Daradich et al.* [2008] showed that the present Martian rotation pole is stable, as expected, with a

revised partitioning into equilibrium and nonequilibrium contributions (hereafter nonequilibrium theory). We extend their analysis in several ways. First, *Daradich et al.* [2008] focused on two degree-2 spherical harmonic gravity coefficients (C_{20} and C_{22}), while we consider all the degree-2 spherical harmonic coefficients. Second, *Daradich et al.* [2008] used the Tharsis center location estimated by *Zuber and Smith* [1997]. The latter study adopts the traditional partitioning of the gravitational figure, while we calculate the location of the Tharsis center using a method that is independent of the adopted partitioning. Third, in addition to finding best fit solutions, we calculate probability density functions for the thickness of the elastic lithosphere, Tharsis' size and location, and the paleopole location given the observed spherical harmonic gravity coefficients. Finally, we consider the effect of the equilibrium and nonequilibrium contributions on the Martian gravity field and shape.

[3] Gravitational field observations have been used to argue for large true polar wander (TPW), a change in the orientation of a planet relative to its rotation vector, driven

¹Department of Earth and Planetary Science, University of California, Berkeley, California, USA.

Table 1. Unnormalized Degree-2 Spherical Harmonic Gravity Coefficients^a

	Observed	Nonhydrostatic	Tharsis	Nonhydrostatic Without Tharsis
C_{20}	-1.95661×10^{-3}	-1.17397×10^{-4}	-1.12676×10^{-4}	-4.72074×10^{-6}
C_{21}	4.73087×10^{-10}	4.73087×10^{-10}	-1.00048×10^{-5}	1.00053×10^{-5}
S_{21}	-9.40775×10^{-11}	-9.40775×10^{-11}	-2.51793×10^{-5}	2.51792×10^{-5}
C_{22}	-5.46322×10^{-5}	-5.46322×10^{-5}	-4.21264×10^{-5}	-1.25058×10^{-5}
S_{22}	3.15871×10^{-5}	3.15871×10^{-5}	3.97535×10^{-5}	-8.16638×10^{-6}

^aWe use the Jet Propulsion Laboratory Mars gravity field MRO95A [Zuber, 2008]. The nonhydrostatic coefficients are calculated assuming a 6% nonhydrostatic contribution to C_{20} . The Tharsis spherical harmonic coefficients are calculated using equation (4) with $C_{20}^T = 2.34857 \times 10^{-4}$, $\theta_T = 90^\circ - 6.67^\circ$, and $\phi_T = 248.33^\circ$. The last column is calculated by removing the Tharsis coefficients from the nonhydrostatic coefficients.

by the mass distribution associated with the emplacement of Tharsis [Zuber and Smith, 1997; Sprenke et al., 2005]. However, these studies adopt the traditional partitioning of the gravitational figure into hydrostatic and nonhydrostatic contributions. Our probability density functions for the paleopole longitude and latitude provide revised constraints on the possible TPW driven by the formation of Tharsis.

2. Traditional Partitioning of the Gravitational Figure

[4] We expand the gravity field at a point with spherical coordinates (r, θ, ϕ) in spherical surface harmonics as

$$\Phi = \frac{GM}{r} + \frac{GM}{r} \sum_{\ell=1}^{\infty} \sum_{m=0}^{\ell} \left(\frac{R}{r}\right)^{\ell} P_{\ell m}(\cos \theta) [C_{\ell m} \cos m\phi + S_{\ell m} \sin m\phi], \quad (1)$$

where G is the gravitational constant, M is the planet mass, R is the mean planetary radius, $P_{\ell m}$ is the associated Legendre function, and $C_{\ell m}$ and $S_{\ell m}$ are spherical harmonic coefficients. We adopt the sign convention of geodesy and astronomy in which the gravitational potential is positive, and the following definition for the associated Legendre functions [e.g., Arfken and Weber, 1995],

$$P_{\ell m}(x) = (1-x^2)^{m/2} \frac{d^m}{dx^m} P_{\ell}(x), \quad (2)$$

where P_{ℓ} is a Legendre polynomial. We use the Jet Propulsion Laboratory Mars gravity field MRO95A [Zuber, 2008]. The unnormalized degree-2 spherical harmonic coefficients are listed in Table 1.

[5] Given the unnormalized degree-2 spherical harmonic coefficients, the total inertia tensor can be written as [e.g., Lambeck, 1980]

$$I_{ij} = I_0 \delta_{ij} + MR^2 \begin{pmatrix} \frac{1}{3}C_{20} - 2C_{22} & -2S_{22} & -C_{21} \\ -2S_{22} & \frac{1}{3}C_{20} + 2C_{22} & -S_{21} \\ -C_{21} & -S_{21} & -\frac{2}{3}C_{20} \end{pmatrix}, \quad (3)$$

where δ_{ij} is the Kronecker delta and I_0 is a spherically symmetric contribution that is not constrained by the spherical harmonic coefficients. Replacing the observed spherical harmonic coefficients (Table 1) in equation (3) and diagonalizing the inertia tensor yields a maximum principal axis that is nearly aligned with the present rotation axis (the offset is $< 2 \times 10^{-5}$ degrees), as expected.

[6] Using the nonhydrostatic theory, Sprenke et al. [2005] estimated the most stable rotation pole location prior to the emplacement of Tharsis by diagonalizing the nonhydrostatic

inertia tensor without contributions associated with Tharsis. They followed the numerical procedure of Zuber and Smith [1997] to remove Tharsis' contribution to the nonhydrostatic gravity field and inertia tensor assuming a 6% nonhydrostatic Tharsis contribution to the spherical harmonic coefficient C_{20} . This is in the range estimated by Bills and James [1999], $\sim 5\text{--}7\%$, based on the observed precession rate and the nonhydrostatic theory.

[7] We revisit the analysis of Sprenke et al. [2005] to illustrate the apparent instability of the present rotational state in the framework of the nonhydrostatic theory, and to validate an analytic method for removing Tharsis contributions from the gravity field that will be used in the following sections. Assuming that Tharsis is axisymmetric at long wavelengths, we can characterize the direct and deformational Tharsis contributions to the gravity field with the spherical harmonic coefficients for the case when the symmetry axis is aligned with the z axis, $C_{\ell 0}^{T,TD}$. Note that $C_{\ell m}^{T,TD} = 0$ for $m \neq 0$ by symmetry in this case. We use the ‘‘T’’ and ‘‘TD’’ superscripts to identify Tharsis and deformational effects of Tharsis, respectively. The spherical harmonic coefficients for the case with the Tharsis center at an arbitrary location with spherical coordinates (θ_T, ϕ_T) are given by

$$\begin{bmatrix} C_{\ell m}^{T,TD} \\ S_{\ell m}^{T,TD} \end{bmatrix} = C_{\ell 0}^{T,TD} (2 - \delta_{m0}) \frac{(\ell - m)!}{(\ell + m)!} P_{\ell m}(\cos \theta_T) \begin{bmatrix} \cos(m\phi_T) \\ \sin(m\phi_T) \end{bmatrix}, \quad (4)$$

where we use the addition theorem for spherical harmonics (e.g., equation (12.171) [Arfken and Weber, 1995, p.746]) and δ_{m0} is the Kronecker delta. For each spherical harmonic degree ℓ , we can find the best fit $C_{\ell 0}^{T,TD}$ by finding the minimum of the misfit function,

$$f(C_{\ell 0}^T) = \sum_{m=0}^{\ell} \left[(C_{\ell m}^{NH} - C_{\ell m}^{T,TD})^2 + (S_{\ell m}^{NH} - S_{\ell m}^{T,TD})^2 \right], \quad (5)$$

where $C_{\ell m}^{NH}$ and $S_{\ell m}^{NH}$ are the nonhydrostatic spherical harmonic coefficients. We minimize equation (5) with Mathematica implementations of the downhill simplex and simulated annealing methods [e.g., Press et al., 1992, chapter 10]. Following Sprenke et al. [2005], if we assume a 6% nonhydrostatic contribution to the observed C_{20} (the other coefficients are 100% nonhydrostatic) and the Tharsis center location estimated by Zuber and Smith [1997] (248.33°E , 6.67°N) minimization of equation (5) yields $C_{20}^T = 2.34857 \times 10^{-4}$. The corresponding degree-2 spherical harmonic coefficients for the Tharsis center at 248.33°E , 6.67°N can be found using equation (4) and are listed in Table 1.

[8] The nonhydrostatic spherical harmonic coefficients after removing Tharsis' contribution are also listed in Table 1.

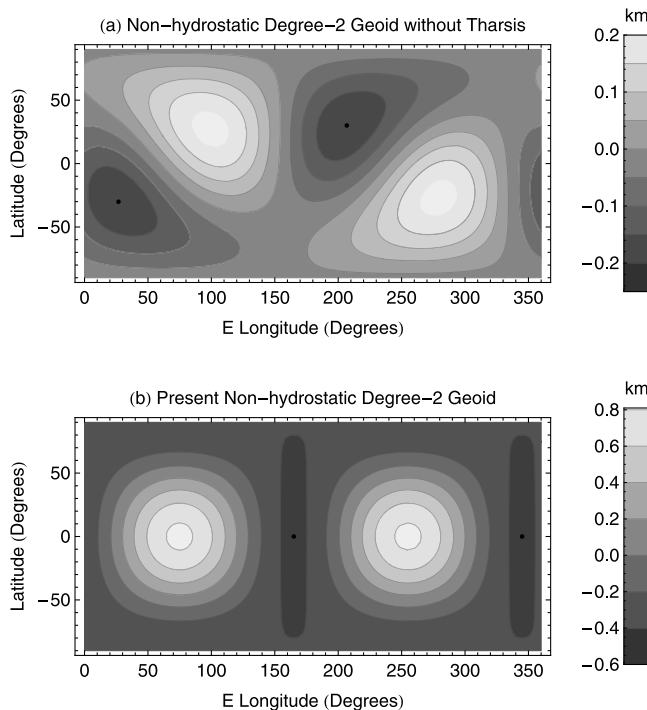


Figure 1. Nonhydrostatic degree-2 geoid (a) without and (b) with Tharsis using the spherical harmonic coefficients in Table 1. The black points show the location of the geoid minima and correspond to the rotation poles.

Replacing these spherical harmonic coefficients in equation (3) and diagonalizing the inertia tensor to calculate the maximum principal axis orientation and the corresponding paleopole location prior to the emplacement of Tharsis yields 206.8°E , 30.1°N . Figure 1a shows the nonhydrostatic geoid (areoid) without Tharsis using the same spherical harmonic coefficients. The geoid minima in Figure 1a correspond to the location of the paleopole and the antipodal pole. Our estimated paleopole location in the framework of the nonhydrostatic theory is in agreement with the numerical result of *Sprenke et al.* [2005] (210°E , 30°N).

[9] *Bills and James* [1999] argued that the finite rigidity of Mars complicates the traditional partitioning into hydrostatic and nonhydrostatic contributions. They noted an apparent instability of the present Martian rotational state when this traditional partitioning is adopted. However, *Sprenke et al.*

[2005] did not consider implications for the present rotational state. In the traditional nonhydrostatic theory, the present rotation pole location is determined by all the nonhydrostatic contributions, including those associated with Tharsis. The nonhydrostatic spherical harmonic coefficients assuming a 6% nonhydrostatic contribution to C_{20} are listed in Table 1. Replacing these spherical harmonic coefficients in equation (3) and diagonalizing the inertia tensor to calculate the maximum principal axis orientation and the corresponding present rotation pole location yields 165.0°E , 0°N . Figure 1b shows the nonhydrostatic geoid, including Tharsis contributions, using the same spherical harmonic coefficients. Once again, the geoid minima in Figure 1b correspond to the two rotation poles. As *Bills and James* [1999] noted, the equatorial location of the maximum principal axis implies that the present-day rotational state is unstable. The apparent instability is due to the neglect of stabilization by the remnant rotational figure supported by the elastic lithosphere [*Willemann*, 1984; *Matsuyama et al.*, 2006].

3. Revised Partitioning of the Gravitational Figure

[10] If the presence of an elastic lithosphere is taken into account using the nonequilibrium theory, the gravitational figure can be partitioned into equilibrium and nonequilibrium contributions [*Daradich et al.*, 2008]. We illustrate the sequence of events and physics that underlies this partitioning in Figure 2. The initial planetary figure is established when there is no lithosphere (Figure 2a), and the elastic lithosphere forms through cooling of the interior (Figure 2b). Lithosphere formation does not disturb the initial planetary figure since the lithosphere forms in an unstressed state. Thus, the planetary figure in Figures 2a and 2b is identical. The mass redistribution associated with loading by Tharsis reorients the planet (Figure 2c), and this reorientation generates elastic stresses within the lithosphere which introduce a memory of the original planetary figure. The postreorientation figure can be separated into equilibrium and nonequilibrium contributions (Figure 2d). The equilibrium contribution is associated with the postreorientation rotational figure. The nonequilibrium contribution is dominated by Tharsis and a remnant rotational figure supported by the elastic lithosphere. The elastic lithospheric thickness continues to increase through cooling of the interior (Figure 2e). Similar to the transition depicted in Figures 2a and 2b, lithospheric thick-

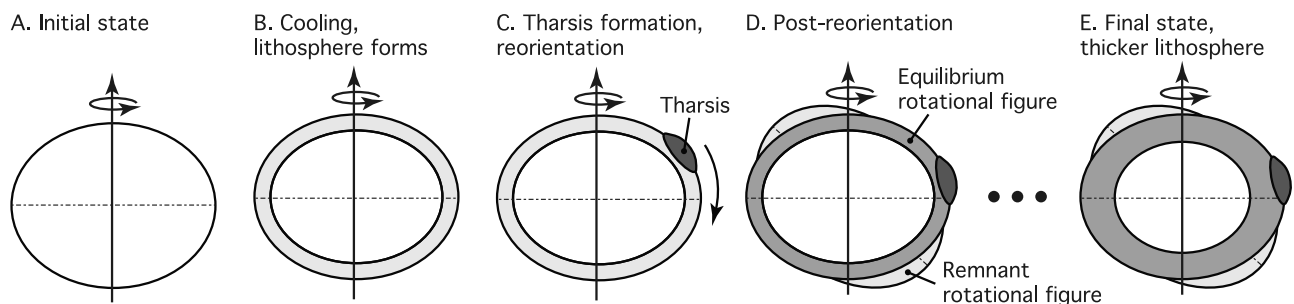


Figure 2. Schematic illustration of the sequence of events and physics that underlies the partitioning of Mars' figure into equilibrium and nonequilibrium contributions.

Table 2. Reference Mars Model Parameter Values^a

Layer	R (km)	ρ (kg m ⁻³)	μ (GPa)
1	1400	7200	0
2	2000	4300	155
3	2400	4100	120
4	3190	3600	80
5	3390	3000	45

^aColumns correspond to layer number, outer radius, density, and shear modulus.

ening does not disturb the planetary figure since the new lithosphere forms in an unstressed state. Thus, the planetary figure in Figures 2d and 2e is identical, and the equilibrium and nonequilibrium contributions must be calculated assuming the elastic lithospheric thickness at the time of loading by Tharsis.

[11] *Daradich et al.* [2008] showed that the present Martian rotational state is stable when the partitioning into equilibrium and nonequilibrium contributions is adopted, and we will not repeat this analysis here. For Mars, the nonequilibrium gravitational figure has contributions from Tharsis, a remnant rotational figure supported by the elastic lithosphere, and any excess contributions. Thus, the degree-2 spherical harmonic coefficients can be written as

$$\begin{aligned} C_{2m} &= C_{2m}^{EQ} + C_{2m}^{RR} + C_{2m}^{T,TD} + C_{2m}^{EX} \\ S_{2m} &= S_{2m}^{EQ} + S_{2m}^{RR} + S_{2m}^{T,TD} + S_{2m}^{EX}, \end{aligned} \quad (6)$$

where we use the superscripts “EQ,” “RR,” “T,TD,” and “EX” to identify equilibrium, remnant rotational figure, Tharsis, and excess contributions respectively. Once again, the Tharsis contributions include the deformation of the planet in response to Tharsis, hence the superscript “T,TD.”

[12] In a reference frame with the z axis aligned with the present rotation axis, the only nonzero equilibrium degree-2 spherical harmonic coefficient is

$$C_{20}^{EQ} = -\frac{1}{3}k_2^T \frac{w^2 R^3}{GM}, \quad (7)$$

where k_2^T is the secular degree-2 tidal Love number and w is the final rotation rate. Replacing this spherical harmonic coefficient in equation (3) and setting the other coefficients to zero yields a diagonalized inertia tensor with the maximum principal axis aligned with the rotation axis (z axis), as expected. The dimensionless tidal Love number describes the response to tidal forcings and depends on the planet’s interior structure and rheology. We adopt a five-layer internal structure model similar to the one adopted by *Bills and James* [1999], as described in Table 2. We use the method of *Sabadini and Vermeersen* [2004] to calculate the corresponding Love numbers. Figure 3a shows k_2^T for elastic lithospheric thicknesses in the range 0–200 km.

[13] Remnant rotational figure contributions arise due to changes in rotation rate and/or orientation of the rotation axis. These contributions are associated with the mass distribution that retains a memory for prior rotational states due

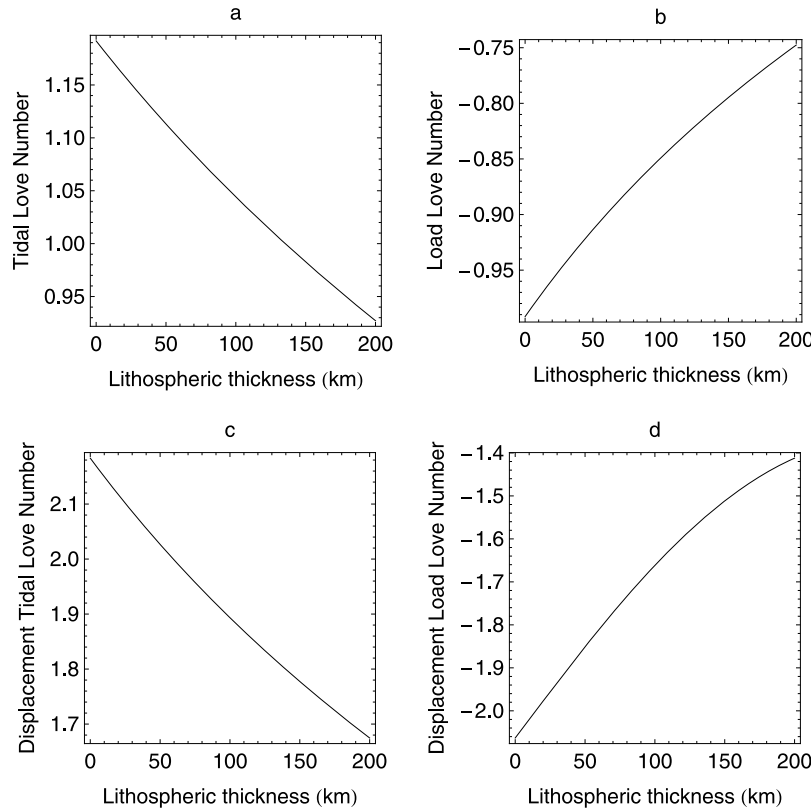


Figure 3. Secular degree-2 (a) tidal Love number, k_2^T ; (b) load Love number, k_2^L ; (c) displacement tidal Love number, h_2^T ; and (d) displacement load Love number, h_2^L as a function of the elastic lithospheric thickness. We adopt the five-layer internal structure model described in Table 2.

to long-term elastic strength. Thus, these contributions are aligned with the initial (prior to reorientation) rotation axis. The remnant rotational figure contributions can be written as [Matsuyama and Nimmo, 2009]

$$\begin{aligned} C_{20}^{RR} &= \frac{1}{6} \left(k_2^{T*} - k_2^T \right) \frac{w_*^2 R^3}{GM} (1 - 3 \cos^2 \theta_R) \\ C_{21}^{RR} &= -\frac{1}{6} \left(k_2^{T*} - k_2^T \right) \frac{w_*^2 R^3}{GM} \sin(2\theta_R) \cos \phi_R \\ S_{21}^{RR} &= -\frac{1}{6} \left(k_2^{T*} - k_2^T \right) \frac{w_*^2 R^3}{GM} \sin(2\theta_R) \sin \phi_R \\ C_{22}^{RR} &= -\frac{1}{12} \left(k_2^{T*} - k_2^T \right) \frac{w_*^2 R^3}{GM} \sin^2 \theta_R \cos(2\phi_R) \\ S_{22}^{RR} &= -\frac{1}{12} \left(k_2^{T*} - k_2^T \right) \frac{w_*^2 R^3}{GM} \sin^2 \theta_R \sin(2\phi_R), \end{aligned} \quad (8)$$

where k_2^{T*} is the secular (or fluid limit) degree-2 tidal Love number for the case without an elastic lithosphere, w_* is the initial rotation rate, and θ_R and ϕ_R are the spherical coordinates for the initial rotation pole. The remnant rotational figure is established in response to loading by Tharsis. Thus, the degree-2 tidal Love number for the case with an elastic lithosphere in equations (7) and (8), k_2^T , must be calculated assuming the elastic lithospheric thickness at the time of loading by Tharsis. Replacing the spherical harmonic coefficients for the remnant rotational figure in equation (3) and diagonalizing the inertia tensor yields a maximum principal axis aligned with the initial rotation axis, as expected.

[14] Given an interior structure model and the corresponding Love numbers, there are two unknowns for the spherical harmonic coefficients of the remnant rotational figure (the initial rotation pole coordinates) and five unknown degree-2 spherical harmonic coefficients of Tharsis. Thus, even if we ignore any excess contributions, there are five constraints (the observed degree-2 spherical harmonic coefficients) and seven unknowns, and the system is underdetermined. Assuming that Tharsis is predominantly axisymmetric at long wavelengths, the total degree-2 spherical harmonic coefficients, excluding excess contributions, can be written as (ignoring terms associated with tidal deformation [Matsuyama and Nimmo, 2009])

$$\begin{aligned} C_{20} &= -\frac{1}{3} k_2^T \frac{w_*^2 R^3}{GM} - \frac{1}{6} \left(k_2^{T*} - k_2^T \right) \frac{w_*^2 R^3}{GM} \\ &\quad \cdot [Q(1 - 3 \cos^2 \theta_T) - (1 - 3 \cos^2 \theta_R)] \\ C_{21} &= \frac{1}{6} \left(k_2^{T*} - k_2^T \right) \frac{w_*^2 R^3}{GM} [Q \sin(2\theta_T) \cos \phi_T - \sin(2\theta_R) \cos \phi_R] \\ S_{21} &= \frac{1}{6} \left(k_2^{T*} - k_2^T \right) \frac{w_*^2 R^3}{GM} [Q \sin(2\theta_T) \sin \phi_T - \sin(2\theta_R) \sin \phi_R] \\ C_{22} &= \frac{1}{12} \left(k_2^{T*} - k_2^T \right) \frac{w_*^2 R^3}{GM} [Q \sin^2 \theta_T \cos(2\phi_T) - \sin^2 \theta_R \cos(2\phi_R)] \\ S_{22} &= \frac{1}{12} \left(k_2^{T*} - k_2^T \right) \frac{w_*^2 R^3}{GM} [Q \sin^2 \theta_T \sin(2\phi_T) - \sin^2 \theta_R \sin(2\phi_R)], \end{aligned} \quad (9)$$

where θ_T and ϕ_T are the spherical coordinates of the Tharsis center. Tharsis' size is given by the dimensionless load size

$$Q \equiv -\frac{C_{20}^{T,TD'}}{C_{20}^{RR'}} = C_{20}^{T'} \left(\frac{1 + k_2^L}{k_2^{T*} - k_2^T} \right) \frac{3GM}{w_*^2 R^3}, \quad (10)$$

where $C_{20}^{T'}$ is the (uncompensated) Tharsis spherical harmonic coefficient for the case when the symmetry axis is aligned with the z axis. Since we assume that Tharsis is axisymmetric, the excess contributions include nonaxisymmetric Tharsis contributions. In equation (10), k_2^L is the secular degree-2 load Love number for the case with an elastic lithosphere, and the factor of $1 + k_2^L$, where $k_2^L < 0$, accounts for the deformation due to Tharsis loading. Figure 3b shows k_2^L for elastic lithospheric thicknesses in the range 0–200 km.

4. Tharsis Center Location and Size

[15] Zuber and Smith [1997] estimated the Tharsis center location (248.33°E, 6.67°N) using the nonhydrostatic theory and assuming a 5% contribution to the observed spherical harmonic coefficient C_{20} . Once again, in the nonhydrostatic theory, the partitioning of the gravitational figure into hydrostatic and nonhydrostatic contributions leads to an apparent instability of the present-day rotational state. If we take into account the presence of an elastic lithosphere using the nonequilibrium theory, we can calculate the nonequilibrium contribution to C_{20} by subtracting the equilibrium contribution (equation (7)) from the observed value. This yields nonequilibrium contributions of 7%, 13%, and 19% for elastic lithospheric thickness of 0, 50, and 100 km, respectively. Our estimate for the case with no elastic lithosphere, 7%, is consistent with the estimate of Bills and James [1999], ~5%–7%, using the nonhydrostatic theory, as expected since there is no remnant rotational figure in this case.

[16] Although it is possible to find best fit solutions for the paleopole location (θ_R and ϕ_R), Tharsis size (Q), and the Tharsis center location (θ_T and ϕ_T) simultaneously using the method described in the following section, the problem is greatly simplified if the Tharsis center location and/or size are known a priori. The equilibrium and remnant rotational figure contributions to the gravity field are limited to spherical harmonic degree 2. Thus, the spherical harmonic coefficients for higher degrees ($\ell > 2$) can be written as

$$\begin{aligned} C_{\ell m} &= C_{\ell m}^{T,TD} + C_{\ell m}^{EX} \\ S_{\ell m} &= S_{\ell m}^{T,TD} + S_{\ell m}^{EX}, \end{aligned} \quad (11)$$

where we use the “T,” “TD,” and “EX” superscripts to identify Tharsis, deformational effects of Tharsis, and excess contributions respectively. Since there are no equilibrium and remnant rotational figure contributions, we can assume that Tharsis dominates the degree-3 gravity field. In this case, assuming an axisymmetric Tharsis and using the addition theorem for spherical harmonics (equation (4)), $\tan \phi_T \sim S_{31}/C_{31}$, $\tan(2\phi_T) \sim S_{32}/C_{32}$, and $\tan(3\phi_T) \sim S_{33}/C_{33}$. Using the MRO95A spherical harmonic coefficients [Zuber, 2008], this yields $\phi_T = 261^\circ$, 256° , and 252° for the order 1, 2, and 3 spherical harmonic coefficients respectively. These simple estimates are in good agreement with each other and with the observed Tharsis center location, validating our assumption that an axisymmetric Tharsis dominates the degree-3 gravity field.

[17] The simplest assumption for the degree-3 excess contributions in equation (11), including nonaxisymmetric Tharsis contributions, is that they represent random perturbations. In this case, we can find best fit solutions for the

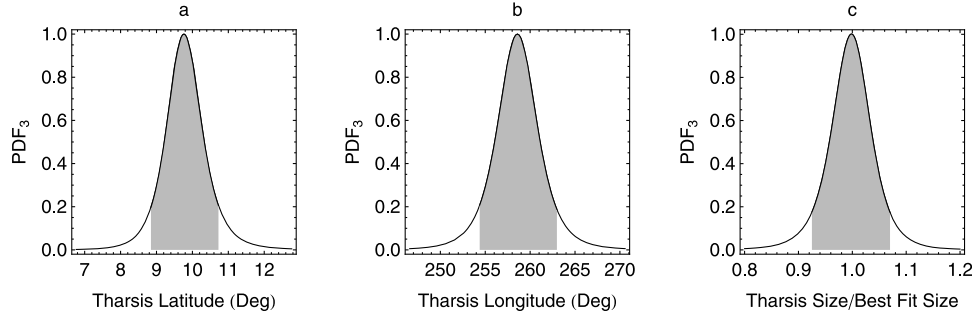


Figure 4. Probability density function (PDF) for Tharsis' (a) latitude, (b) longitude, and (c) size calculated using equation (16). The shaded region encloses the smallest 90% confidence interval.

Tharsis center location and size by minimizing the misfit function

$$\chi_3 = \sum_{m=0}^3 \left[(C_{3m}^{OBS} - C_{3m}^{T,TD})^2 + (S_{3m}^{OBS} - S_{3m}^{T,TD})^2 \right]. \quad (12)$$

[18] In equation (12), C_{3m}^{OBS} and S_{3m}^{OBS} are the observed spherical harmonic coefficients, and the predicted degree-3 Tharsis coefficients, $C_{3m}^{T,TD}$ and $S_{3m}^{T,TD}$, are given by equation (4). The latter are functions of a single spherical harmonic coefficient ($C_{30}^{T,TD}$) and the Tharsis center location (θ_T and ϕ_T). Since we assume an axisymmetric Tharsis, the symmetry axes for the degree-2 and the degree-3 gravity field associated with Tharsis are the same. Minimization of equation (12) yields a best fit solution with $C_{30}^{T,TD} = 1.3055 \times 10^{-4}$, $\theta_T = 80.2^\circ$ and $\phi_T = 258.6^\circ$. This estimate of the Tharsis center longitude agrees with the simple estimate above using the ratio between spherical harmonic coefficients.

[19] We can extend equation (12) to consider higher degree spherical harmonic coefficients. Assuming that Tharsis is predominantly axisymmetric up to degree 5, we can find best fit solutions for the Tharsis center location and spherical harmonic coefficients by minimizing the misfit function

$$\chi_{3-5} = \sum_{\ell=3}^5 \sum_{m=0}^{\ell} \left[(C_{\ell m}^{OBS} - C_{\ell m}^{T,TD})^2 + (S_{\ell m}^{OBS} - S_{\ell m}^{T,TD})^2 \right]. \quad (13)$$

[20] Minimization of equation (13) yields $\theta_T = 80.5^\circ$, $\phi_T = 257.3^\circ$, $C_{30}^{T,TD} = 1.31603 \times 10^{-4}$, $C_{40}^{T,TD} = 5.28363 \times 10^{-5}$, and $C_{50}^{T,TD} = -2.13278 \times 10^{-5}$. These best fit solutions are in agreement with the solutions described above using the degree-3 spherical harmonic coefficients alone, validating our assumption that Tharsis is predominantly axisymmetric at long wavelengths. Our results are not sensitive to the particular spherical harmonic degree chosen for the truncation in equation (13). For example, choosing degree 6 as the truncation degree yields $\theta_T = 80.6^\circ$, $\phi_T = 257.2^\circ$, $C_{30}^{T,TD} = 1.32316 \times 10^{-4}$, $C_{40}^{T,TD} = 5.25002 \times 10^{-5}$, $C_{50}^{T,TD} = -2.15358 \times 10^{-5}$, and $C_{60}^{T,TD} = -2.19211 \times 10^{-5}$.

[21] Unless otherwise stated, we adopt the method for finding the best fit Tharsis parameters based on the degree-3 spherical harmonic coefficients alone throughout the rest of the paper. The probability density function (PDF) for the observed degree-3 spherical harmonic coefficients given the Tharsis spherical harmonic coefficient ($C_{30}^{T,TD}$) and the Tharsis center location (θ_T and ϕ_T) is proportional to $\chi_3^{-N/2}$,

where $N = 7$ is the number of degree-3 spherical harmonic coefficients [Sivia and Skilling, 2006, section 8.2]:

$$\text{PDF}_3(C_{3m}, S_{3m} | C_{30}^{T,TD}, \theta_T, \phi_T) \propto \chi_3^{-7/2}. \quad (14)$$

[22] Using Bayes' theorem [Sivia and Skilling, 2006], the PDF for the unknown model parameters ($C_{30}^{T,TD}$, θ_T , and ϕ_T) given the observed spherical harmonic coefficients is also proportional to $\chi_3^{-N/2}$ if we assume a uniform distribution for the prior PDF($C_{30}^{T,TD}$, θ_T , ϕ_T). Thus,

$$\text{PDF}_3(C_{30}^{T,TD}, \theta_T, \phi_T | C_{3m}, S_{3m}) \propto \chi_3^{-7/2}. \quad (15)$$

[23] Note that this PDF is independent of the thickness of the elastic lithosphere since there are no equilibrium or remnant rotational figure contributions to the degree-3 gravity field. Using marginalization [Sivia and Skilling, 2006], the PDFs for the Tharsis colatitude, longitude, and spherical harmonic coefficient given the observed degree-3 spherical harmonic coefficients are given by

$$\begin{aligned} \text{PDF}_3(\theta_T | C_{3m}, S_{3m}) &\propto \int \text{PDF}(C_{30}^{T,TD}, \theta_T, \phi_T | C_{3m}, S_{3m}) dC_{30}^{T,TD} d\phi_T \\ \text{PDF}_3(\phi_T | C_{3m}, S_{3m}) &\propto \int \text{PDF}(C_{30}^{T,TD}, \theta_T, \phi_T | C_{3m}, S_{3m}) dC_{30}^{T,TD} d\theta_T, \\ \text{PDF}_3(C_{30}^{T,TD} | C_{3m}, S_{3m}) &\propto \int \text{PDF}(C_{30}^{T,TD}, \theta_T, \phi_T | C_{3m}, S_{3m}) d\theta_T d\phi_T \end{aligned} \quad (16)$$

respectively. We assume $0 < \theta_T < 180^\circ$ and $0 < \phi_T < 360^\circ$ for the Tharsis center location integration domains, and a finite domain around the best fit $C_{30}^{T,TD} = 1.3055 \times 10^{-4}$. The PDFs in equation (16) are shown in Figure 4. The maxima of the PDFs represent the most likely values given the observed degree-3 spherical harmonic coefficients and coincide with the parameters of the best fit solution $C_{30}^{T,TD} = 1.3055 \times 10^{-4}$, $\theta_T = 80.2^\circ$ and $\phi_T = 258.6^\circ$. The area under the PDF between two values is proportional to how much we believe the parameter of interest is in that range. The shaded regions in Figure 4 enclose the smallest 90% confidence interval: $79.3^\circ < \theta_T < 81.2^\circ$ and $254.4^\circ < \phi_T < 262.8^\circ$.

5. Paleopole Location and Thickness of the Elastic Lithosphere

[24] The degree-2 gravity field has equilibrium, remnant rotational figure, Tharsis, and excess contributions

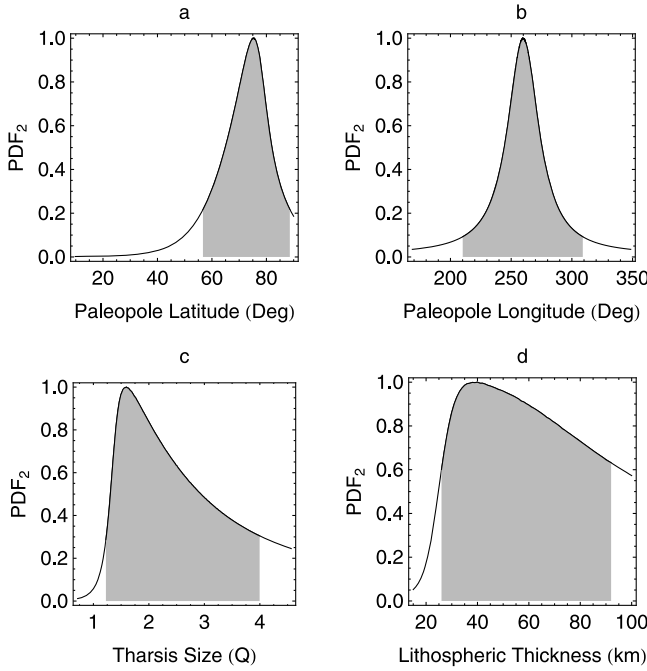


Figure 5. Probability density function for the paleopole (a) latitude and (b) longitude, (c) Tharsis size, and (d) the elastic lithospheric thickness. The shaded region encloses the smallest 90% confidence interval.

(equation (6)). Similar to the degree-3 excess contributions, given our assumption of axisymmetry for Tharsis, the excess contributions also include Tharsis perturbations from axisymmetry. Once again, the simplest assumption for the excess contributions is that they represent random perturbations. Under this assumption, we can find best fit solutions by minimizing the misfit function

$$\chi_2 \equiv \sum_{m=0}^2 (C_{2m}^{OBS} - C_{2m})^2 + \sum_{m=1}^2 (S_{2m}^{OBS} - S_{2m})^2. \quad (17)$$

[25] In equation (17), C_{2m}^{OBS} and S_{2m}^{OBS} are the observed spherical harmonic coefficients, and C_{2m} and S_{2m} are the predicted spherical harmonic coefficients for the equilibrium, remnant rotational figure, and Tharsis contributions given by equation (9). The predicted spherical harmonic coefficients are functions of the Tharsis size and location (Q , θ_T , and ϕ_T), the paleopole location (θ_R and ϕ_R), and the degree-2 Love numbers, which in turn depend on the elastic lithospheric thickness (T_e). We ignore rotation rate variations. Given the Tharsis center location inferred using the degree-3 gravity field ($\theta_T = 80.2^\circ$ and $\phi_T = 258.6^\circ$), we find best fit solutions for the degree-2 gravity field by minimizing equation (17) with respect to Tharsis size (Q) and the paleopole location (θ_R and ϕ_R).

[26] The probability density function (PDF) for the unconstrained model parameters (T_e , Q , θ_R , and ϕ_R) given the observed degree-2 spherical harmonic coefficients (C_{2m} and S_{2m}) and the Tharsis center location (θ_T and ϕ_T) is proportional to $\chi_2^{-N/2}$, where $N = 5$ is the number of degree-2

spherical harmonic coefficients [Sivia and Skilling, 2006, section 8.2],

$$\text{PDF}_2(T_e, Q, \theta_R, \phi_R | C_{2m}, S_{2m}, \theta_T, \phi_T) \propto \chi_2^{-5/2}. \quad (18)$$

[27] In equation (18), χ_2 is given by equation (17) and we use Bayes' theorem [Sivia and Skilling, 2006] under the assumption of a uniform distribution for the prior $\text{PDF}(T_e, Q, \theta_R, \phi_R)$ over a specified interval. Since the Love numbers in equation (9) are functions of the elastic lithospheric thickness (T_e), we highlight this dependency in equation (18).

[28] Using marginalization [Sivia and Skilling, 2006], the PDFs for the elastic lithospheric thickness, Tharsis size, and the paleopole colatitude and longitude are given by

$$\begin{aligned} & \text{PDF}_2(T_e | C_{2m}, S_{2m}, \theta_T, \phi_T) \\ & \propto \int \text{PDF}_2(T_e, Q, \theta_R, \phi_R | C_{2m}, S_{2m}, \theta_T, \phi_T) dQ d\theta_R d\phi_R \\ & \text{PDF}_2(Q | C_{2m}, S_{2m}, \theta_T, \phi_T) \\ & \propto \int \text{PDF}_2(T_e, Q, \theta_R, \phi_R | C_{2m}, S_{2m}, \theta_T, \phi_T) dT_e d\theta_R d\phi_R \\ & \text{PDF}_2(\theta_R | C_{2m}, S_{2m}, \theta_T, \phi_T) \\ & \propto \int \text{PDF}_2(T_e, Q, \theta_R, \phi_R | C_{2m}, S_{2m}, \theta_T, \phi_T) dT_e dQ d\phi_R \\ & \text{PDF}_2(\phi_R | C_{2m}, S_{2m}, \theta_T, \phi_T) \\ & \propto \int \text{PDF}_2(T_e, Q, \theta_R, \phi_R | C_{2m}, S_{2m}, \theta_T, \phi_T) dT_e dQ d\theta_R. \quad (19) \end{aligned}$$

[29] We adopt the following integration domains for the paleopole location: $0 \leq \theta_R < 90^\circ$ and $\phi_T - 90^\circ \leq \phi_R \leq \phi_T + 90^\circ$.

[30] Turcotte *et al.* [2002] estimate a global average elastic lithospheric thickness $T_e = 90 \pm 10$ km using correlations between gravity anomalies and topography. This estimate includes topography that formed at various times and the thickness of the elastic lithosphere generally increases with time [Zuber *et al.*, 2000; McKenzie *et al.*, 2002; McGovern *et al.*, 2004], as expected due to cooling. Therefore, we adopt 100 km as a conservative upper limit. As we will show below, the PDF for the elastic lithospheric thickness approaches zero as T_e approaches ~ 15 km (Figure 5d). Thus, we adopt 15 km as a reasonable lower limit.

[31] We estimate the Tharsis size integration domain using the degree-3 spherical harmonic coefficient associated with Tharsis, $C_{30}^{T,TD}$, and assuming a surface density distribution for Tharsis [Willemann, 1984],

$$\sigma(\theta) = \begin{cases} \frac{\sigma_0}{2} \left[\cos\left(\frac{\theta}{\psi}\right) + 1 \right], & \theta \leq \psi \\ 0, & \theta > \psi, \end{cases} \quad (20)$$

where σ_0 is the surface density at the center ($\theta = 0$) and ψ is the angular radius of Tharsis. The value of σ_0 is not important since it drops out of equation (22) below. The degree-2 and degree-3 spherical harmonic coefficients associated with Tharsis and the deformation of the planet in response to loading by Tharsis are given by

$$\begin{aligned} C_{20}^{T,TD} &= (1 + k_2^l) \frac{2\pi R^2}{M} \int_0^\psi d\theta \sin\theta P_{20}(\cos\theta) \sigma(\theta) \\ C_{30}^{T,TD} &= (1 + k_3^l) \frac{2\pi R^2}{M} \int_0^\psi d\theta \sin\theta P_{30}(\cos\theta) \sigma(\theta), \end{aligned} \quad (21)$$

where k_2^L and k_3^L are the secular degree-2 and degree-3 load Love numbers. Thus, the normalized degree-2 Tharsis size (equation (10)) can be written as

$$Q = C_{30}^{T,TD} \left(\frac{1+k_2^L}{1+k_3^L} \right) \left(\frac{1}{k_2^{T*} - k_2^T} \right) \frac{3GM}{w_*^2 R^3} \frac{\int_0^\psi d\theta \sin\theta P_{20}(\cos\theta)\sigma(\theta)}{\int_0^\psi d\theta \sin\theta P_{30}(\cos\theta)\sigma(\theta)}. \quad (22)$$

[32] Assuming an angular radius $\psi = 35^\circ$ for Tharsis yields $0.7 < Q < 4.6$ for elastic lithospheric thicknesses in the range 15–100 km. This estimate requires assuming a particular surface density distribution; however, our results are not sensitive to the adopted Tharsis size integration domain.

[33] Figure 5 shows the PDF for the paleopole location, Tharsis size, and thickness of the elastic lithosphere using equation (19). The maximum of the PDF represents the most likely value: $\theta_R = 14.8^\circ$, $\phi_R = 259.5^\circ$, $Q = 1.6$, and $T_e = 40$ km. The area under the PDF between two values is proportional to how much we believe the parameter of interest is in that range. The shaded regions in Figure 5 enclose the smallest 90% confidence interval: $1.4^\circ < \theta_R < 33.3^\circ$, $210.0^\circ < \phi_R < 309.0^\circ$, $1.2 < Q < 4.0$, and $26 \text{ km} < T_e < 92 \text{ km}$. Although the maximum of the PDF indicates the single most probable value for the parameter of interest X , the weighted average,

$$\bar{X} \equiv \frac{\int X \text{PDF}_2 dX}{\int \text{PDF}_2 dX}, \quad (23)$$

or expected value, is more representative since it takes into account the asymmetry of the PDF. The expected values are $\theta_R = 18.9^\circ$, $\phi_R = 259.5^\circ$, $Q = 2.5$, and $T_e = 58$ km. Note that the expected and most likely values for the paleopole longitude are identical since the PDF is symmetric about the maximum (Figure 5b). Similarly, the expected and most likely values for the PDFs of Tharsis' location (Figure 4) are identical.

[34] Assuming an axisymmetric Tharsis and ignoring excess contributions at spherical harmonic degree 2, rotational stability requires the paleopole longitude to be equal to the Tharsis center longitude [Matsuyama *et al.*, 2007]. The expected paleopole longitude, 259.5° , and Tharsis center longitude, 258.6° , nearly satisfy this; validating our assumption of a predominantly axisymmetric Tharsis and small excess contributions to the gravitational figure. Similarly, under the same assumptions, rotational stability requires [Matsuyama *et al.*, 2007],

$$\theta_R = \frac{1}{2} \sin^{-1} \left[\frac{Q}{\beta} \sin(2\theta_T) \right], \quad (24)$$

where

$$\beta \sim 1 + \frac{32\pi}{5} \mu T_e \left(\frac{1+\nu}{5+\nu} \right) \left(\frac{R^3}{GM^2} \right) \left(\frac{h_2^{T^2}}{k_2^{T*} - k_2^T} \right) \quad (25)$$

quantifies the stabilizing effect of the elastic energy in the lithosphere by reducing the effective Tharsis size. In equation (25), μ , ν , and T_e are the shear modulus, Poisson's ratio, and thickness of the elastic lithosphere respectively; and h_2^T is the secular degree-2 displacement tidal Love

number (Figure 3c). Assuming $\nu = 0.25$ and $\mu = 45$ GPa (Table 2) and replacing the expected values; $Q = 2.5$, $\theta_T = 80.2^\circ$, and $T_e = 58$ km; in equations (24) and (25) yields $\beta \sim 1.5$ and $\theta_R = 16.4^\circ$; which is slightly smaller than the expected paleopole colatitude, 18.9° . The small discrepancy could be due to small excess contributions, including non-axisymmetric Tharsis contributions. There are two possible solutions for the paleopole colatitude in equation (24), 16.4° and $90^\circ - 16.4^\circ = 73.6^\circ$, both of which are consistent with rotational stability given Tharsis' size and colatitude. Our analysis provides an independent constraint that favors the small TPW solution.

6. Gravity Field

[35] Figure 6 shows the observed geoid and illustrates the effect of removing the equilibrium rotational figure, Tharsis, and the remnant rotational figure. We use the Jet Propulsion Laboratory Mars gravity field MRO95A [Zuber, 2008]. It is useful to consider the degree-2 geoid alone since the equilibrium and remnant rotational figure only affect the degree-2 geoid. Figure 6a shows the observed degree-2 geoid. For the expected thickness of the elastic lithosphere, $T_e = 58$ km, $k_2^T = 1.10$ (Figure 3a), and the only nonzero equilibrium degree-2 spherical harmonic coefficient is $C_{20}^{EQ} = -1.68468 \times 10^{-3}$ (equation (7)). We calculate the Tharsis and remnant rotational figure spherical harmonic coefficients using equation (9) with the expected model parameters ($T_e = 58$ km, $Q = 2.5$, $\theta_T = 80.2^\circ$, $\phi_T = 258.6^\circ$, $\theta_R = 18.9^\circ$, and $\phi_R = 259.5^\circ$) and ignoring equilibrium contributions. Table 3 lists the degree-2 Tharsis and remnant rotational figure spherical harmonic coefficients.

[36] The equilibrium rotational figure dominates the observed degree-2 geoid (Figure 6a). The degree-2 nonequilibrium geoid (Figure 6b), calculated by removing the equilibrium rotational figure from the observed degree-2 geoid, is dominated by Tharsis. The nonequilibrium geoid is not fully centered around Tharsis due to the remnant rotational figure and excess contributions. The remnant rotational figure becomes visible after removal of Tharsis from the nonequilibrium geoid (Figure 6c). Figure 6d shows the excess geoid; that is, the nonequilibrium geoid without the Tharsis and remnant rotational figure contributions. The excess contributions are smaller than the nonequilibrium contributions, dominated by the Tharsis and remnant rotational figure, by roughly an order of magnitude. The excess geoid is offset with respect to the Tharsis geoid, as expected if it represents excess contributions that are not associated with an axisymmetric Tharsis. Once again, the excess geoid includes nonaxisymmetric Tharsis contributions. There is no clear correlation between the degree-2 excess geoid and the Elysium rise or the Utopia, Isidis, or Hellas basins.

[37] Following the method of section 4, we find best fit solutions for the Tharsis spherical harmonic coefficients at degree ℓ by minimizing the misfit function,

$$\chi_\ell = \sum_{m=0}^{\ell} \left[(C_{\ell m}^{OBS} - C_{\ell m}^{T,TD})^2 + (S_{\ell m}^{OBS} - S_{\ell m}^{T,TD})^2 \right], \quad (26)$$

where $C_{\ell m}^{OBS}$ and $S_{\ell m}^{OBS}$ are the observed coefficients and $C_{\ell m}^{T,TD}$ and $S_{\ell m}^{T,TD}$ are the Tharsis coefficients given by equation (4). Minimization of equation (26) given the expected (and most

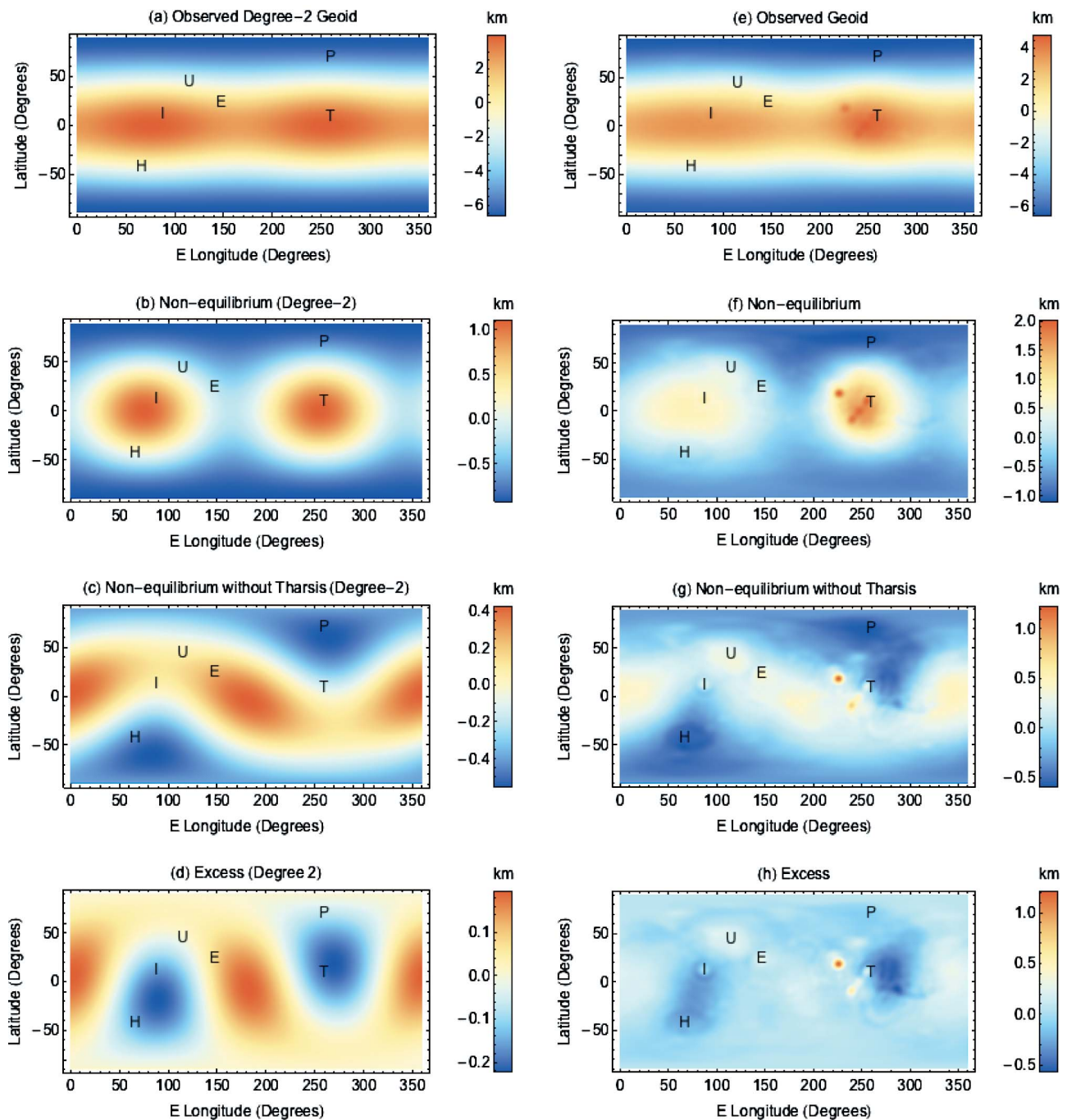


Figure 6. (a) Observed degree-2 geoid (areoid) and the same geoid (b) without the equilibrium rotational figure, (c) without the equilibrium rotational figure and Tharsis, and (d) without the equilibrium rotational figure, Tharsis, and the remnant rotational figure. (e) Observed geoid up to degree and order 40 and the same geoid (f) without the equilibrium rotational figure, (g) without the equilibrium rotational figure and Tharsis, and (h) without the equilibrium rotational figure, Tharsis and the remnant rotational figure. We use the Jet Propulsion Laboratory Mars gravity field MRO95A [Zuber, 2008]. The centers for the Tharsis and Elysium rise and the Utopia, Isidis, and Hellas basins are indicated by the corresponding first letter. The paleopole location is indicated by the letter P.

likely) Tharsis center location (258.6°E , 9.8°N) yields the following spherical harmonic coefficients for the case with Tharsis at the pole ($\theta_T = 0$): $C_{30}^{T,TD'} = 1.3055 \times 10^{-4}$, $C_{40}^{T,TD'} = 5.32303 \times 10^{-5}$, and $C_{50}^{T,TD'} = -2.10345 \times 10^{-5}$. The corresponding coefficients for the case with the Tharsis center at

the expected location (258.6°E , 9.8°N) can be found using equation (4) and are listed in Table 4. We characterize Tharsis with spherical harmonics up to degree 5 since higher degree harmonics introduce features that are clearly not associated with an axisymmetric Tharsis centered at 258.6°E ,

Table 3. Degree-2 Spherical Harmonic Coefficients for the Tharsis and the Remnant Rotational Figure Contributions to the Gravity Field

ℓ	m	Tharsis		Remnant Rotational Figure	
		$C_{\ell m}$	$S_{\ell m}$	$C_{\ell m}$	$S_{\ell m}$
2	0	-1.57321×10^{-4}		-1.16144×10^{-4}	
2	1	-1.1424×10^{-5}	-5.66568×10^{-5}	7.69775×10^{-6}	4.15333×10^{-5}
2	2	-7.7116×10^{-5}	3.24166×10^{-5}	3.37541×10^{-6}	-1.2957×10^{-6}

9.8°N. Our results are not significantly changed if Tharsis is characterized with higher degree spherical harmonics since the misfit function (equation (26)) yields small spherical harmonic coefficients in this case.

[38] Figures 6e–6h show the observed geoid up to degree and order 40 and illustrate the effect of removing the equilibrium rotational figure, Tharsis, and the remnant rotational figure. We remove axisymmetric Tharsis contributions up to degree and order 5 using the spherical harmonic coefficients in Tables 3 and 4. Similar to the degree-2 nonequilibrium geoid (Figure 6b), the total nonequilibrium geoid (Figure 6f) is not fully centered around Tharsis due to the remnant rotational figure and excess contributions. The remnant rotational figure becomes visible after removal of Tharsis from the nonequilibrium geoid (Figure 6g). Shorter wavelength geological features (e.g., the Elyisum rise and the Utopia, Isidis, and Hellas basins) become more visible with the removal of the long wavelength geoid associated with the equilibrium, Tharsis, and the remnant rotational figure contributions (Figure 6h).

7. Shape

[39] The equilibrium rotational figure, Tharsis, and the remnant rotational figure also affect the shape of Mars. We expand the radius at a point with spherical coordinates (θ, ϕ) in spherical surface harmonics as

$$r(\theta, \phi) = \sum_{\ell=0}^{\infty} P_{\ell m}(\cos \theta) [c_{\ell m} \cos(m\phi) + s_{\ell m} \sin(m\phi)], \quad (27)$$

Table 4. Spherical Harmonic Coefficients for the Tharsis Contribution to the Gravity Field and Shape to Degree and Order 5^a

ℓ	m	Gravity		Shape	
		$C_{\ell m}$	$S_{\ell m}$	$c_{\ell m}$ (m)	$s_{\ell m}$ (m)
3	0	-3.17219×10^{-5}		-494.594	
3	1	5.43608×10^{-6}	2.69599×10^{-5}	84.7569	420.347
3	2	-4.97279×10^{-6}	2.09037×10^{-6}	-77.5335	32.5921
3	3	2.9256×10^{-6}	4.30489×10^{-6}	45.6147	67.1199
4	0	1.43738×10^{-5}		259.794	
4	1	1.23406×10^{-6}	6.12024×10^{-6}	22.3045	110.618
4	2	1.58276×10^{-6}	-6.65329×10^{-7}	28.607	-12.0253
4	3	2.03039×10^{-7}	2.98763×10^{-7}	3.66977	5.3999
4	4	1.82899×10^{-7}	-1.8677×10^{-7}	3.30574	-3.37571
5	0	-5.82909×10^{-6}		-118.296	
5	1	3.13432×10^{-7}	1.55445×10^{-6}	6.3608	31.5461
5	2	-3.65795×10^{-7}	1.53766×10^{-7}	-7.42345	3.12053
5	3	4.35589×10^{-8}	6.4095×10^{-8}	0.883986	1.30075
5	4	-1.23018×10^{-8}	1.25622×10^{-8}	-0.249653	0.254938
5	5	8.53697×10^{-9}	5.54397×10^{-9}	0.17325	0.11251

^aSee Tables 3 and 5 for the degree-2 coefficients.

where $c_{\ell m}$ and $s_{\ell m}$ are spherical harmonic coefficients. The only nonzero spherical harmonic coefficient for the equilibrium rotational figure can be written as

$$c_{20}^{EQ} = -R h_2^T \frac{w^2 R^3}{3GM}, \quad (28)$$

where h_2^T is the secular degree-2 displacement tidal Love number. For the expected thickness of the elastic lithosphere, $\bar{T}_e = 58$ km, $h_2^T = 2.00$ (Figure 3c) and $c_{20}^{EQ} = -10422.9$ m. Similarly, the spherical harmonic coefficient for the remnant rotational figure for the case when the initial rotation axis is aligned with the z axis can be written as

$$c_{20}^{RR} = -R \left(h_2^{T*} - h_2^T \right) \frac{w_*^2 R^3}{3GM}, \quad (29)$$

where $h_2^{T*} = 2.18$ (Figure 3c) is the secular degree-2 displacement tidal Love number for the case without an elastic lithosphere and w_* is the initial rotation rate. Ignoring rotation rate variations, $c_{20}^{RR} = -933.204$ m for the expected thickness of the elastic lithosphere, $\bar{T}_e = 58$ km. The spherical harmonic coefficients for the case with the initial rotation axis at the expected location; $\theta_R = 18.9^\circ$ and $\phi_R = 259.5^\circ$; are given by

$$\begin{bmatrix} c_{2m}^{RR} \\ s_{2m}^{RR} \end{bmatrix} = c_{20}^{RR} (2 - \delta_{m0}) \frac{(2-m)!}{(2+m)!} P_{2m}(\cos \theta_R) \begin{bmatrix} \cos(m\phi_R) \\ \sin(m\phi_R) \end{bmatrix}, \quad (30)$$

where we use the addition theorem for spherical harmonics. These spherical harmonic coefficients are listed in Table 5.

[40] Assuming an axisymmetric Tharsis aligned with the z axis, the spherical harmonic coefficients for the planet deformation in response to loading by Tharsis can be written as

$$c_{\ell 0}^{TD} = R h_{\ell}^L C_{\ell 0}^T, \quad (31)$$

where h_{ℓ}^L is the secular degree- ℓ displacement load Love number (Figure 3d) and $C_{\ell 0}^T$ is the gravity spherical harmonic coefficient for the direct contribution of Tharsis. The

Table 5. Degree-2 Spherical Harmonic Coefficients for the Tharsis and the Remnant Rotational Figure Contributions to the Shape

ℓ	m	Tharsis		Remnant Rotational Figure	
		$c_{\ell m}$ (m)	$s_{\ell m}$ (m)	$c_{\ell m}$ (m)	$s_{\ell m}$ (m)
2	0	-1947.04		-786.333	
2	1	-141.386	-701.195	52.1164	281.195
2	2	-954.402	401.194	22.8527	-8.77231

gravity and shape spherical harmonic coefficients for the direct Tharsis contribution, $C_{\ell 0}^T$ and $C_{\ell 0}^{T'}$, are related by

$$C_{\ell 0}^{T'} = \frac{4\pi R^2}{M(2\ell + 1)} \rho c_{\ell 0}^{T'}, \quad (32)$$

where ρ is the density of the Tharsis load. Thus, the spherical harmonic coefficients for the total Tharsis contribution to the topography, including the planet deformation due to loading and for the case when the symmetry axis is aligned with the z axis, can be written as

$$c_{\ell 0}^{T,TD'} = \frac{C_{\ell 0}^{T,TD'}}{1 + k_{\ell}^L} \left[\frac{M(2\ell + 1)}{4\pi R^2 \rho} + R h_{\ell}^L \right]. \quad (33)$$

[41] In equation (33), $C_{\ell 0}^{T,TD'} = (1 + k_{\ell}^L) C_{\ell 0}^{T'}$ are the spherical harmonic coefficients for the gravity field associated with Tharsis and the planet deformation in response to loading by Tharsis. Assuming a Tharsis load density $\rho = 3 \text{ g cm}^{-3}$; the expected elastic lithospheric thickness, $\bar{T}_e = 58 \text{ km}$; and the gravity spherical harmonic coefficients found in section 6 in equation (33) yields $c_{20}^{T,TD'} = 4264.74 \text{ m}$, $c_{30}^{T,TD'} = 2035.48 \text{ m}$, $c_{40}^{T,TD'} = 962.093 \text{ m}$, and $c_{50}^{T,TD'} = -426.876 \text{ m}$. The spherical harmonic coefficients for the case with the Tharsis center at the expected location; $\bar{\theta}_T = 80.2^\circ$ and $\bar{\phi}_R = 258.6^\circ$; are given by

$$\begin{bmatrix} c_{\ell m}^{T,TD'} \\ s_{\ell m}^{T,TD'} \end{bmatrix} = c_{\ell 0}^{T,TD'} (2 - \delta_{m0}) \frac{(\ell - m)!}{(\ell + m)!} P_{\ell m}(\cos \bar{\theta}_T) \begin{bmatrix} \cos(m\bar{\phi}_T) \\ \sin(m\bar{\phi}_T) \end{bmatrix}, \quad (34)$$

where we use the addition theorem for spherical harmonics. These spherical harmonic coefficients are listed in Table 4.

[42] Once again, it is useful to focus on the degree-2 topography since the equilibrium and remnant rotational figure are limited to degree 2. Figure 7a shows the observed degree-2 topography and Figures 7b–7d illustrate the effect of removing the equilibrium rotational figure, Tharsis, and the remnant rotational figure. The degree-2 geoid and topography for these contributions are correlated and show many similarities. First, the equilibrium rotational figure dominates the observed degree-2 topography (Figure 7a). Second, the nonequilibrium topography is dominated by Tharsis, but it is not fully centered around Tharsis due to the remnant rotational figure and excess contributions (Figure 7b). Third, the remnant rotational figure becomes visible after removal of Tharsis from the nonequilibrium topography (Figure 7c). Fourth, the excess topography is offset with respect to the Tharsis topography, as expected (Figure 7d). Finally, there is no clear correlation between the degree-2 excess topography and the Elysium rise or the Utopia, Isidis, or Hellas basins. The most notable difference between the degree-2 geoid and the degree-2 topography is an offset of the excess contributions (compared Figures 6d and 7d).

[43] Figures 7e–7f show the observed topography up to degree and order 40 and also illustrate the effect of removing the equilibrium rotational figure, Tharsis, and the remnant rotational figure. We remove axisymmetric Tharsis contributions up to degree and order 5 using the spherical harmonic coefficients in Tables 4 and 5. Similar to the observed geoid (Figure 6e), the equilibrium rotational figure dominates

the observed topography (Figure 7e). However, while the nonequilibrium geoid is dominated by Tharsis (Figure 6f), the nonequilibrium topography is dominated by both Tharsis and the north-south dichotomy (Figure 7f). Similarly, while the remnant rotational figure is visible in the nonequilibrium geoid without Tharsis (Figure 6g), the nonequilibrium topography without Tharsis is dominated by the north-south dichotomy and the remnant rotational figure is not visible (Figure 7g). The absence of the north-south dichotomy in the degree-2 topography (Figures 7b–7d) is expected since it is approximately a degree-1 feature. This can be illustrated by considering a simple model. If we assume a height distribution,

$$h(\theta) = \begin{cases} -h_0, & \theta \leq \psi \\ 0, & \theta > \psi, \end{cases} \quad (35)$$

where ψ is the angular radius of the northern lowlands, the only nonzero degree-2 shape coefficient is

$$c_{20} = -\frac{5}{4} h_0 \cos \psi \sin^2 \psi, \quad (36)$$

which approaches zero as ψ approaches 90° .

8. Summary and Discussion

[44] We have used the Martian gravity field to calculate probability density functions for Tharsis' size and location, the paleopole location prior to the formation of Tharsis, and the thickness of the elastic lithosphere at the time of loading. We adopt a revised theory in which the gravitational field is partitioned into equilibrium and nonequilibrium contributions [Daradich *et al.*, 2008; Matsuyama and Nimmo, 2009]. We illustrate the sequence of events and the physics that underlies this partitioning in Figure 2. Unlike the traditional partitioning into hydrostatic and nonhydrostatic contributions, which is generally not appropriate for planets with an elastic lithosphere, the revised partitioning is consistent with present rotational stability.

[45] Given the observed degree-3 spherical harmonic coefficients, the expected (and most likely) Tharsis center location is $258.6 \pm 4.2^\circ\text{E}$, $9.8 \pm 0.9^\circ\text{N}$, where the uncertainties represent the smallest 90% confidence interval (Figure 4). This location is different from the location estimated by Zuber and Smith [1997] (248.33°E , 6.67°N). However, the latter estimate is based on the traditional partitioning of the planet figure into hydrostatic and nonhydrostatic contributions. The finite rigidity of Mars complicates this traditional partitioning and leads to an apparent instability of the present rotational state [Bills and James, 1999]. We estimate the Tharsis center location using the degree-3 gravity field and assuming that Tharsis is predominantly axisymmetric at long wavelengths. Our method is independent of the particular partitioning assumed since the degree-3 gravity field does not contain contributions associated with the rotational figure.

[46] Given the Tharsis center location and the observed degree-2 spherical harmonic coefficients, the expected elastic lithospheric thickness is $58_{-32}^{+34} \text{ km}$ (Figure 5d). Turcotte *et al.* [2002] estimated $90 \pm 10 \text{ km}$ for the global average elastic lithospheric thickness using correlations between gravity anomalies and topography. We estimate the elastic litho-

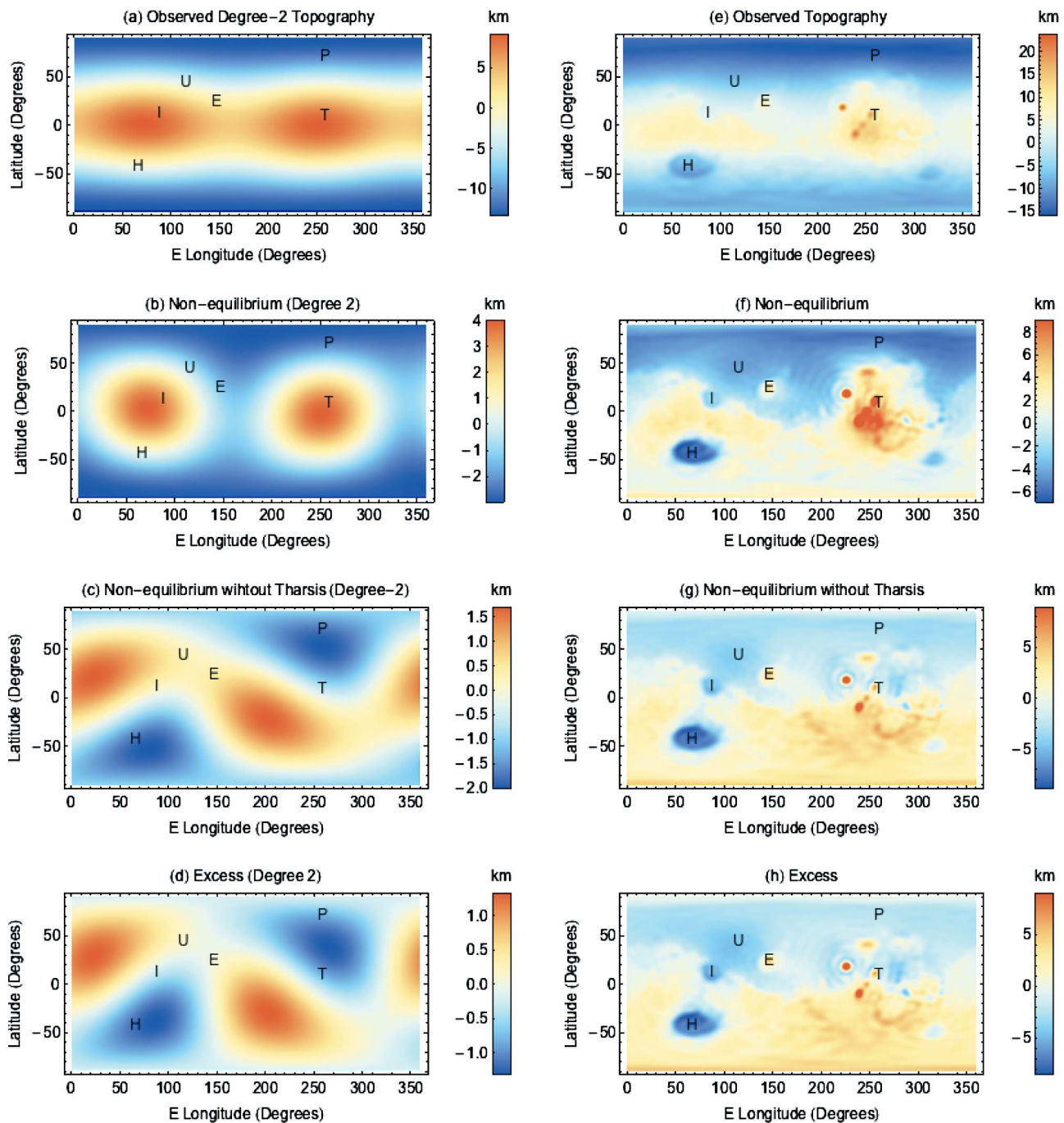


Figure 7. (a) Observed degree-2 topography and the same topography (b) without the equilibrium rotational figure, (c) without the equilibrium rotational figure and Tharsis, and (d) without the equilibrium rotational figure, Tharsis, and the remnant rotational figure. (e) Observed topography up to degree and order 40 and the same topography (f) without the equilibrium rotational figure, (g) without the equilibrium rotational figure and Tharsis, and (h) without the equilibrium rotational figure, Tharsis, and the remnant rotational figure. We use Mars Orbiting Laser Altimetry (MOLA) data. The centers for the Tharsis and Elysium rise and the Utopia, Isidis, and Hellas basins are indicated by the corresponding first letter. The paleopole location is indicated by the letter P.

spheric thickness at the time Tharsis was emplaced, while the estimate of *Turcotte et al.* [2002] includes topography that formed after Tharsis. Since the thickness of the elastic lithosphere generally increases with time [Zuber *et al.*, 2000; McKenzie *et al.*, 2002; McGovern *et al.*, 2004], as expected

due to cooling, our estimated thickness is expected to be smaller than the estimate of *Turcotte et al.* [2002]. Our estimate is consistent with the estimate of *Jellinek et al.* [2008] for the elastic lithospheric thickness at the time of Tharsis uplift, ≈ 40 km, on the basis of joint consideration of

magnetic field anomalies and dynamic topography around Tharsis.

[47] Given the Tharsis center location and the observed degree-2 spherical harmonic gravity coefficients, the expected paleopole location prior to the emplacement of Tharsis is $259.5 \pm 49.5^\circ\text{E}$, $71.1^{+17.5^\circ}_{-14.4^\circ}\text{N}$ (Figures 5a–5b). This paleopole location lies within a degree of a great circle passing through the center of Tharsis and the present pole, as expected for any TPW driven by the emplacement of an axisymmetric Tharsis. The expected amount of TPW, $18.9^{+14.4^\circ}_{-17.5^\circ}$, also agrees well with the amount of TPW estimated on the basis of rotational stability, 16.4° , given the expected Tharsis size, $\bar{Q} = 2.5$ (Figure 5c), and Tharsis center colatitude, $\theta_T = 80.2^\circ$ (Figure 4a).

[48] The expected paleopole location ($259.5 \pm 49.5^\circ\text{E}$, $71.1^{+17.5^\circ}_{-14.4^\circ}\text{N}$) is significantly different from the estimate of *Sprenke et al.* [2005] (210°E , 30°N) also inferred using the degree-2 gravity field. However, the latter study adopts the traditional partitioning of the planet figure into hydrostatic and nonhydrostatic contributions. Once again, the finite rigidity of Mars complicates this traditional partitioning and leads to an apparent instability of the present rotational state [*Bills and James*, 1999]. As illustrated in Figure 2, we use a revised partitioning into equilibrium and nonequilibrium contributions that takes into account finite rigidity [*Daradich et al.*, 2008; *Matsuyama and Nimmo*, 2009]. This partitioning is consistent with a present Martian rotational state that is stable [*Daradich et al.*, 2008].

[49] Several observations have been used to infer that large TPW occurred on Mars. These observations include the distributions of large impact craters that may have traced ancient equatorial satellites [*Schultz and Lutz-Garihan*, 1982]; the resemblance between equatorial and polar sediments [*Schultz and Lutz*, 1988]; and magnetic paleopole locations estimated using crustal magnetic anomalies [*Arkani-Hamed and Boutin*, 2004; *Hood et al.*, 2005]. Our estimate for the paleopole location implies 18.9° of expected TPW, and $<33.3^\circ$ of TPW with 90% confidence, driven by the formation of Tharsis. Since Tharsis is the dominant mass anomaly capable of driving large TPW, our constraint on the amount of TPW is not consistent with the large TPW suggested by previous studies.

[50] The expected paleopole location ($259.5 \pm 49.5^\circ\text{E}$, $71.1^{+17.5^\circ}_{-14.4^\circ}\text{N}$) agrees with the estimate of *Mutch et al.* [1976] (250°E , 75°N), based on the global distribution of valley networks, assuming that they trace the paleoequator. However, *Phillips et al.* [2001] concluded that the location and orientation of many of the valley networks was controlled by, and hence postdate, Tharsis. In this case, the valley networks are not expected to trace the paleoequator prior to TPW driven by the formation of Tharsis.

[51] Recent studies suggest TPW subsequent to the formation of Tharsis and our constraint for TPW driven by the emplacement of Tharsis has implications for these studies. *Perron et al.* [2007] show that the long wavelength deformation of putative shorelines [*Clifford and Parker*, 2001] can be explained by $30\text{--}60^\circ$ of TPW. Similarly, *Kite et al.* [2009] illustrate that the $5\text{--}10^\circ$ offset between paleopole deposits and the present rotation axis can be explained by TPW. In both studies, the inferred TPW path is approximately 90° from the center of Tharsis, as expected for a post-Tharsis TPW if Tharsis remains the dominant mass

anomaly. *Perron et al.* [2007] and *Kite et al.* [2009] found that surface loads can explain the inferred TPW paths. However, the size of the loads necessary to drive the inferred TPW depends on the prior TPW driven by Tharsis and both studies required a large TPW driven by Tharsis. Our constraint of a small TPW event driven by Tharsis precludes the possibility that the surface loads considered by *Perron et al.* [2007] and *Kite et al.* [2009] were responsible for the post-Tharsis TPW. Ancient internal or surface loads that no longer have observable signatures are required to explain the inferred post-Tharsis TPW. The present rotation pole, the pre-Tharsis paleopole, and the center of Tharsis lie within a degree of the same great circle. This close alignment requires that other surface or internal loads no longer represent significant mass anomalies, otherwise the alignment would be broken.

[52] The total nonequilibrium geoid is dominated by Tharsis (Figure 6f). Our estimated Tharsis center does not coincide with the center of the nonequilibrium geoid (Figure 6f) because the nonequilibrium geoid also contains remnant rotational figure and excess contributions. The remnant rotational figure becomes visible with the removal of Tharsis (Figure 6g). Removal of the long wavelength contributions of the equilibrium rotational figure, Tharsis, and the remnant rotational figure improves the visibility of shorter wavelength geological features (Figure 6h).

[53] The nonequilibrium topography is dominated by Tharsis and the north-south dichotomy (Figure 7f). Unlike the nonequilibrium geoid, the remnant rotational figure does not become visible with the removal of Tharsis due to the strong signal associated with the north-south dichotomy (Figure 7g). Instead, the nonequilibrium topography without Tharsis reveals a better defined north-south dichotomy boundary (Figure 7g) similar to the elliptical boundary seen in the crustal thickness maps of *Andrews-Hanna et al.* [2008].

[54] **Acknowledgments.** We acknowledge support from the Miller Institute for Basic Research and NASA grant NNX09AN18G.

References

- Andrews-Hanna, J. C., M. T. Zuber, and W. B. Banerdt (2008), The borealis basin and the origin of the Martian crustal dichotomy, *Nature*, *453*, 1212–1215, doi:10.1038/nature07011.
- Arfken, G., and H. Weber (1995), *Mathematical Methods for Physicists*, 4th ed., 952 pp., Academic, Orlando, Fla.
- Arkani-Hamed, J., and D. Boutin (2004), Paleomagnetic poles of Mars: Revisited, *J. Geophys. Res.*, *109*, E03011, doi:10.1029/2003JE002229.
- Bills, B. G., and T. S. James (1999), Moments of inertia and rotational stability of Mars: Lithospheric support of subhydrostatic rotational flattening, *J. Geophys. Res.*, *104*(E4), 9081–9096, doi:10.1029/1998JE900003.
- Clifford, S. M., and T. J. Parker (2001), The evolution of the Martian hydrosphere: Implications for the fate of a primordial ocean and the current state of the northern plains, *Icarus*, *154*, 40–79, doi:10.1006/icar.2001.6671.
- Daradich, A., J. X. Mitrovica, I. Matsuyama, J. T. Perron, M. Manga, and M. A. Richards (2008), Equilibrium rotational stability and figure of Mars, *Icarus*, *194*, 463–475, doi:10.1016/j.icarus.2007.10.017.
- Hood, L. L., C. N. Young, N. C. Richmond, and K. P. Harrison (2005), Modeling of major Martian magnetic anomalies: Further evidence for polar reorientations during the noachian, *Icarus*, *177*, 144–173, doi:10.1016/j.icarus.2005.02.008.
- Jellinek, A. M., C. L. Johnson, and G. Schubert (2008), Constraints on the elastic thickness, heat flow, and melt production at early tharsis from topography and magnetic field observations, *J. Geophys. Res.*, *113*, E09004, doi:10.1029/2007JE003005.
- Kite, E. S., I. Matsuyama, M. Manga, J. T. Perron, and J. X. Mitrovica (2009), True polar wander driven by late-stage volcanism and the distri-

- bution of paleopolar deposits on Mars, *Earth Planet. Sci. Lett.*, *280*, 254–267, doi:10.1016/j.epsl.2009.01.040.
- Lambeck, K. (1980), *The Earth's Variable Rotation: Geophysical Causes and Consequences*, 449 pp., Cambridge Univ. Press, Cambridge.
- Matsuyama, I., and F. Nimmo (2009), Gravity and tectonic patterns of mercury: Effect of tidal deformation, spin-orbit resonance, nonzero eccentricity, despinning, and reorientation, *J. Geophys. Res.*, *114*, E01010, doi:10.1029/2008JE003252.
- Matsuyama, I., J. X. Mitrovica, M. Manga, J. T. Perron, and M. A. Richards (2006), Rotational stability of dynamic planets with elastic lithospheres, *J. Geophys. Res.*, *111*, E02003, doi:10.1029/2005JE002447.
- Matsuyama, I., F. Nimmo, and J. X. Mitrovica (2007), Reorientation of planets with lithospheres: The effect of elastic energy, *Icarus*, *191*, 401–412, doi:10.1016/j.icarus.2007.05.006.
- McGovern, P. J., S. C. Solomon, D. E. Smith, M. T. Zuber, M. Simons, M. A. Wieczorek, R. J. Phillips, G. A. Neumann, O. Aharonson, and J. W. Head (2004), Correction to “localized gravity/topography admittance and correlation spectra on Mars: Implications for regional and global evolution,” *J. Geophys. Res.*, *109*, E07007, doi:10.1029/2004JE002286.
- McKenzie, D., D. N. Barnett, and D.-N. Yuan (2002), The relationship between Martian gravity and topography, *Earth Planet. Sci. Lett.*, *195*(1–2), 1–16, doi:10.1016/S0012-821X(01)00555-6.
- Mutch, T., R. E. Arvidson, J. Head, K. L. Jones, and R. S. Saunders (1976), *The Geology of Mars*, Princeton Univ. Press, Princeton, N. J.
- Perron, J. T., J. X. Mitrovica, M. Manga, I. Matsuyama, and M. A. Richards (2007), Evidence for an ancient Martian ocean in the topography of deformed shorelines, *Nature*, *447*, 840–843, doi:10.1038/nature05873.
- Phillips, R. J., et al. (2001), Ancient geodynamics and global scale hydrology on Mars, *Science*, *291*(5513), 2587–2591, doi:10.1126/science.1058701.
- Press, W. H., S. A. Teukolsky, W. T. Vetterling, and B. P. Flannery (1992), *Numerical Recipes in C. The Art of Scientific Computing*, 2nd ed., 994 pp., Cambridge Univ. Press, Cambridge.
- Sabadini, R., and B. Vermeersen (2004), *Global Dynamics of the Earth: Applications of Normal Mode Relaxation Theory to Solid-Earth Geophysics*, Kluwer Acad., Dordrecht, Netherlands.
- Schultz, P., and A. B. Lutz (1988), Polar wandering of Mars, *Icarus*, *73*, 91–141, doi:10.1016/0019-1035(88)90087-5.
- Schultz, P. H., and A. B. Lutz-Garihan (1982), Grazing impacts on Mars—A record of lost satellites, *Proc. Lunar Planet. Sci. Conf.*, *13th*, Part 1, *J. Geophys. Res.*, *87*, suppl., A84–A96.
- Sivia, D. S., and J. Skilling (2006), *Data Analysis: A Bayesian Tutorial*, 2nd ed., Oxford Univ. Press, New York.
- Sprenke, K. F., L. L. Baker, and A. F. Williams (2005), Polar wander on Mars: Evidence in the geoid, *Icarus*, *174*, 486–489, doi:10.1016/j.icarus.2004.11.009.
- Turcotte, D. L., R. Shcherbakov, B. D. Malamud, and A. B. Kucinskis (2002), Is the Martian crust also the Martian elastic lithosphere?, *J. Geophys. Res.*, *107*(E11), 5091, doi:10.1029/2001JE001594.
- Willemann, R. J. (1984), Reorientation of planets with elastic lithospheres, *Icarus*, *60*, 701–709, doi:10.1016/0019-1035(84)90174-X.
- Zuber, M. T. (2008), Mars reconnaissance orbiter derived gravity data, *MRO-M-RSS-5-SDP-V1.0*, NASA Planet. Data Syst., Greenbelt, Md.
- Zuber, M. T., and D. E. Smith (1997), Mars without tharsis, *J. Geophys. Res.*, *102*(E12), 28,673–28,685, doi:10.1029/97JE02527.
- Zuber, M. T., et al. (2000), Internal structure and early thermal evolution of Mars from Mars global surveyor topography and gravity, *Science*, *287*, 1788–1793, doi:10.1126/science.287.5459.1788.

M. Manga and I. Matsuyama, Department of Earth and Planetary Science, University of California, 307 McCone Hall, Berkeley, CA 94720, USA. (manga@seismo.berkeley.edu; isa@berkeley.edu)